nature communications

Article

https://doi.org/10.1038/s41467-025-64550-4

Nanoscale soft interaction-engineered perovskite heterojunctions for highly efficient and reproducible solar cells

Received: 27 May 2025

Accepted: 20 September 2025

Published online: 28 October 2025

Check for updates

Bo Li[1,2,8] ✉, Danpeng Gao[2,8], Francesco Vanin[2,3,8], Chunlei Zhang[2], Zexin Yu[2], Ning Wang[2], Jie Gong[2], Shuai Li[2], Jianqiu Gong[2], Liangchen Qian[2], Yen-Hung Lin[4], Martin Stolterfoht[5], Nicholas J. Long[3] ✉ & Zonglong Zhu[2,6,7] ✉

The rational design of perovskite heterojunctions is crucial for advancing the efficiency and operational stability of perovskite solar cells (PSCs). However, conventional methods face challenges in precisely controlling interfacial phase purity at the nanoscale and achieving conformal heterojunction coverage. Herein, we report a 'soft-soft' interaction-guided strategy to tailor perovskite heterojunction formation by introducing dimethyl sulfide (DMS) as a soft Lewis base additive in the organic cation solution. The resulting DMS-modulated PSCs achieve a remarkable power conversion efficiency (PCE) of up to 26.70%, with a certified PCE of 26.48%. The devices exhibit exceptional operational stability, retaining over 94% of their initial PCE after 2000 h of maximum power point tracking under continuous 1-sun illumination (ISOS-L-1 protocol). Furthermore, the universality of this 'soft-soft' interaction strategy is validated across a range of diverse perovskite compositions and ligand systems, demonstrating its potential for scalable and reproducible PSC fabrication.

The strategic design of perovskite heterojunctions plays a pivotal role in the advancement of perovskite solar cells (PSCs), offering a means to boost both power conversion efficiency (PCE) and operational stability[1–5]. Engineered through precise interfacial interactions, these tailored heterojunctions provide essential features such as moisture resistance, suppression of ion migration, and surface defect passivation[6–11]. These attributes are crucial for reducing non-radiative recombination, thereby enhancing the performance of the solar cells. However, the effectiveness of these heterojunctions depends on the structural and energetic interfacial landscape formed at the nanoscale, which is influenced by surface coverage and phase uniformity[12]. Controlling these parameters at a molecular and nanoscale level poses a significant challenge, particularly with the conventional in-situ fabrication methods commonly used to fabricate high-efficiency PSCs[13–20]. In this conventional approach, organic ligands interact with the perovskite surface to initiate heterojunction formation involving complex multi-step phase transitions and interactions between solvents and ligands[21,22]. The reaction kinetics in these processes are difficult to control due to the delicate balance required in cation diffusion and exchange[23,24].

This complexity leads to several critical challenges, including the formation of mixed-dimensional phases, inconsistent interfacial

[1]School of Materials Science and Engineering, Central South University, Changsha, China. [2]Department of Chemistry, City University of Hong Kong, Kowloon, Hong Kong SAR, China. [3]Department of Chemistry, Imperial College London, MSRH Building, White City Campus, London, UK. [4]Department of Electronic and Computer Engineering, The Hong Kong University of Science and Technology, Hong Kong, Hong Kong SAR, China. [5]Department Electronic Engineering, Chinese University of Hong Kong, Hong Kong, Hong Kong SAR, China. [6]Shenzhen Research Institute, City University of Hong Kong, Shenzhen, China. [7]Hong Kong Institute for Clean Energy, City University of Hong Kong, Kowloon, Hong Kong SAR, China. [8]These authors contributed equally: Bo Li, Danpeng Gao, Francesco Vanin. ✉e-mail: boli72@csu.edu.cn; n.long@imperial.ac.uk; zonglzhu@cityu.edu.hk

conformality, and morphological and compositional imperfections[12,25,26]. Such interfacial imperfections induce nanoscopic energetic disorder, exacerbating charge trapping and enhancing non-radiative recombination pathways, ultimately compromising device performance and stability[27]. To overcome these limitations, it is essential to move beyond conventional in-situ fabrication methods toward precise and controllable strategies. Specifically, achieving precise control over crystallization kinetics at the molecular level through rational ligand engineering and controlled interfacial interactions relies on carefully selecting ligands with appropriate chemical affinity and donor characteristics.

In this work, we present a soft-soft interaction-guided strategy to modulate perovskite heterojunction interface formation by incorporating the soft Lewis base, dimethyl sulfide (DMS), into ammonium cation precursor solutions. DMS's unique combination of a high donor number (DN), low dielectric constant (DC), and low boiling point (BP) enables dynamic soft-soft interactions between the electron-rich sulfur in DMS and the soft Pb^{2+} ions at the perovskite surface. These interactions selectively steer the formation of a preferred-phase heterojunction while finely modulating nanoscale crystallization kinetics, enabling the growth of conformal, defect-minimized interfaces. The resulting PSCs achieve an outstanding PCE of 26.70% (certified 26.48%), with exceptional operational stability, retaining >94% of initial performance after 2000 h of continuous 1-sun illumination (ISOS-L-1 protocol). Furthermore, this strategy demonstrates broad applicability across various perovskite compositions and ligand systems, underscoring its transformative potential for scalable, high-performance PSC fabrication.

Results

Soft-soft interaction-guided heterojunction construction

We constructed the heterojunction using 3-fluoro-phenethylammonium iodide (3F-PEAI) as the low-dimensional (LD) perovskite precursor, dissolving it in isopropyl alcohol (IPA), and depositing it in-situ onto the surface of the bulk perovskite film $Cs_{0.05}FA_{0.9}MA_{0.05}PbI_3$ (hereafter referred to as "CsFAMA"). During the deposition process, 3F-PEAI interacted with the perovskite surface, inducing the formation of LD perovskite phase based on the 3F-PEA organic spacer, thereby establishing a LD/bulk "3F-PEA/CsFAMA" heterojunction. Notably, as previously reported[21], the formation of the LD layer occurs through a dimensional reduction mechanism, particularly in FA-dominated perovskites, where the sequential intercalation of ammonium ligand cations at the three-dimensional (3D) ($n = \infty$) perovskite surface drives $n = 3 \rightarrow 2 \rightarrow 1$ LD heterojunction growth. Therefore, slowing the reaction rate of this transition is crucial for obtaining high-quality LD perovskite layers with enhanced purity and conformality[21]. This can be achieved by introducing additives that can strongly coordinate with CsFAMA perovskite without disrupting its chemical composition or structure, effectively protecting the delaminated layers from the rapid LD cation intercalation. Moreover, the additives readily evaporate during heterojunction formation, allowing the reaction to reach completion.

Guided by the Hard and Soft Acids and Bases (HSAB) theory, which identifies Pb^{2+} as a soft acid with a strong affinity for soft bases, we strategically selected dimethyl sulfide (DMS) and diethyl sulfide (DES) as representative candidates[28]. As shown in Fig. 1a, compared to IPA, which serves as the solvent for ligands, exhibiting relatively low coordination ability and moderate polarity (with a DN of 21.2 and a DC of 19.9), both DMS and DES demonstrate significantly higher coordination ability (with a DN of 40–41), enabling strong soft-soft interactions with Pb^{2+} on the top layer of bulk perovskite as shown in Fig. 1b. This soft-soft interaction between DMS and Pb^{2+} ions has been proven by Lead-207 Nuclear Magnetic Resonance Spectroscopy (^{207}Pb NMR) and Fourier Transform Infrared (FTIR) Spectroscopy in Supplementary Fig. 1. Moreover, due their low DC (6–7), they cannot dissolve any component of the perovskite structure. In addition, DMS has a low BP of 38 °C, enabling it to volatilize during heterojunction formation, whereas DES exhibits a higher BP than that of IPA, at 91 °C. To clarify the role these properties play in heterojunction formation, we also compared N,N-dimethylformamide (DMF) and dimethyl sulfoxide (DMSO), which have relatively moderate DN (26.6 and 29.8) and high DC and BP values. They have recently been employed as trace additives in LD ligand solutions to control the quantum size of LD layers, with or without the addition of MAI[29–31].

The effect of different additives on the phase selection and purity of the LD layer was first studied using X-ray diffraction (XRD), as shown in Fig. 1c. All films exhibited similar diffraction peaks at $2\theta > 10°$, along with peaks corresponding to the n = 1 and n = 2 phases of 3F-PEA-based LD perovskite, consistent with the films deposited from solutions with stoichiometric ratios of $(3F\text{-}PEA)_2PbI_4$ and $(3F\text{-}PEA)_2(Cs_{0.05}FA_{0.9}MA_{0.05})Pb_2I_7$ (as shown in Supplementary Fig. 2). However, differences emerged depending on the choice of additives. Compared to IPA, the addition of DMF and DMSO produced a dominant n = 1 phase. This can be attributed to their ability to rapidly dissolve the top layer of bulk perovskite and the organic cations, accelerating dimensional reduction (Supplementary Fig. 3). Additionally, owing to the high BP, thicker LD layers are formed, as confirmed by X-ray photoelectron spectroscopy (XPS) depth profiling in Supplementary Fig. 4[29,32]. The increased thickness and the dominance of the n = 1 phase are well known to negatively impact charge transport in complete devices and should be avoided[4]. In contrast, the addition of DMS and DES favored the formation of a dominant n = 2 phase. Unlike DMF and DMSO, these solvents cannot effectively dissolve perovskite or ammonium salts (Supplementary Fig. 5). Instead, they protect the perovskite layer by slowing down the ingression of the organic cations into the intermediate LD phases. Notably, in films prepared with DES, the n = 2 / n = 1 peak intensity ratio was lower than in those prepared with DMS, possibly due to the slower evaporation rate of DES, which hindered the complete conversion to the LD phase. This resulted in poor efficiency, which will be further discussed in the performance section.

To further elucidate the reaction kinetics of LD phase formation, we focused on the heterojunction films fabricated using IPA and IPA + DMS, capturing the in-situ formation process through time-resolved grazing-incidence wide-angle X-ray scattering (GIWAXS) as shown in Fig. 1d–g. The test was conducted by placing the CsFAMA perovskite film, which had been pre-wetted with ligand solution, on a pre-heated holder at 70 °C. The t_0 was taken to be the frame where perovskite diffraction peaks became apparent. In Fig. 1d, e, the formation of 3F-PEA/CsFAMA heterojunction clearly followed a dimensional reduction mechanism whereby the CsFAMA surface was gradually intercalated by the 3F-PEA ligand solution to form a short-lived n = 3 phase (t_1) directly alongside the n = 2 phase before the appearance of the final n = 1 phase (t_2). Then, during the growth stage, the intensity stabilized at t_3, indicating the completion of the LD heterojunction formation (Fig. 1e). This dimensional reduction process is similar to that of previous findings[21]. However, we observed the simultaneous presence of n = 2 and 1 phases, which might be attributed to the introduction of Cs^+ ions[29,33].

Upon introducing DMS, the transition reaction evolved differently, as shown in Fig. 1f, g. Experimental observations revealed that in the early stage (t_1), n = 3 phase formed alone. As the reaction proceeded (t_2), n = 2 and n = 1 phases emerged separately and at a slower rate compared to the pure IPA system. The mechanism involves the high DN of DMS, which engages in soft-soft interactions with Pb^{2+} on the perovskite surface, driven by the strong affinity between the soft base (DMS) and soft acid (Pb^{2+}). These interactions form Pb-DMS complexes that inhibit 3F-PEA$^+$ coordination in the early stages, promoting the formation of the higher n = 3 phase while suppressing intercalation. As DMS gradually volatilizes during the reaction due to its low BP, the Pb-DMS interactions dissociate, re-exposing the Pb^{2+} layers to the organic precursor solution. This controlled release of Pb^{2+}

https://doi.org/10.1038/s41467-025-64550-4

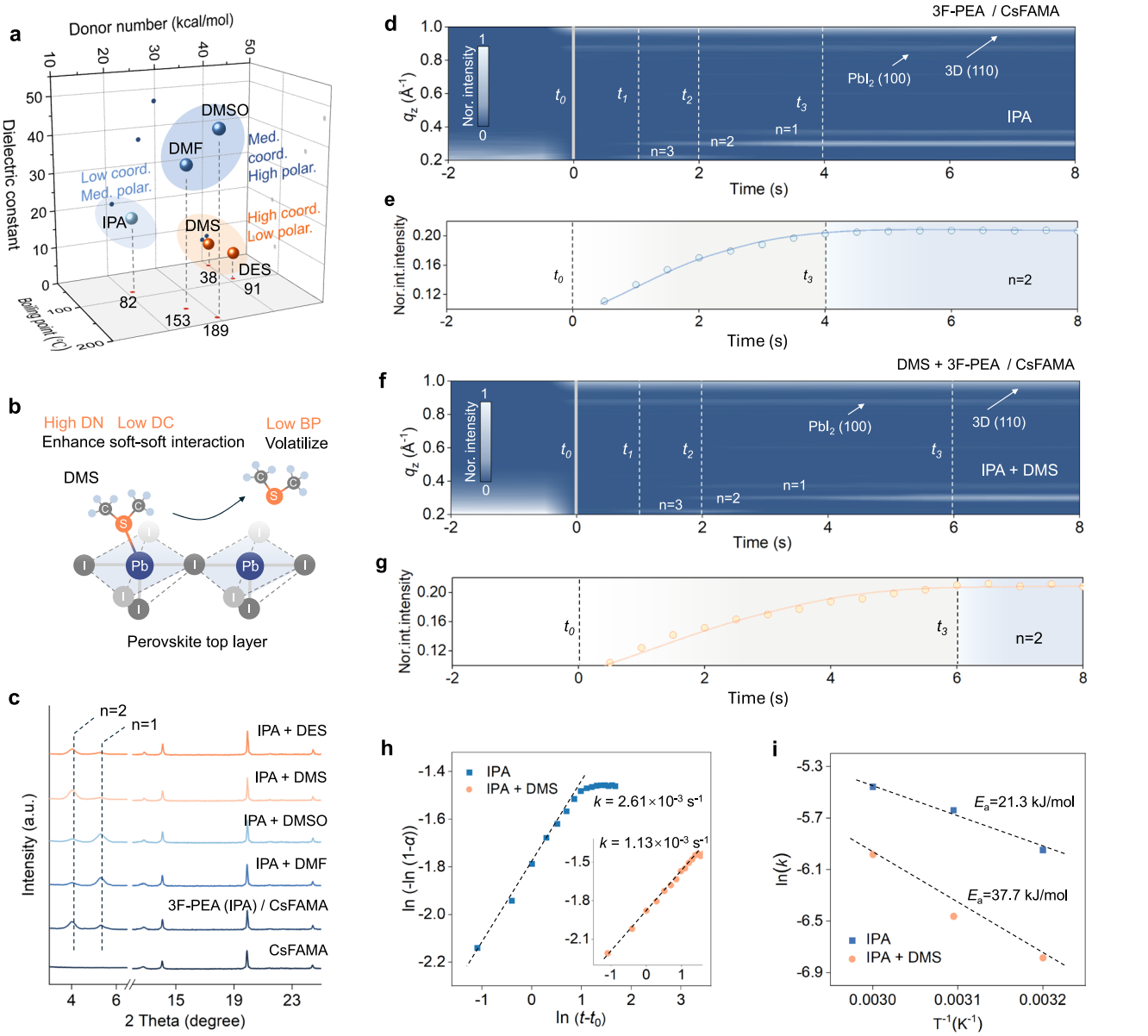

Fig. 1 | Soft-soft interaction-guided heterojunction construction. a Donor number (DN), dielectric constant (DC), and boiling point (BP) of Isopropyl Alcohol (IPA), Dimethylformamide (DMF), Dimethyl Sulfoxide (DMSO), Dimethyl Sulfide (DMS), and Diethyl Sulfide (DES). The shadings highlight the spatial position of the solvent, corresponding to medium coordination and high polarity (Med. coord., High polar.) for DMF and DMSO; low coordination and medium polarity (Low coord., Med. polar.) for IPA; and high coordination with low polarity (High coord., Low polar.) for DMS and DES. **b** Schematic diagram of the soft-soft interaction between DMS (soft base) and Pb^{2+} (soft acid) on the perovskite top layer. Soft-soft interactions refer to the affinity between soft acids and soft bases, as defined by Hard-Soft Acid-Base (HSAB) theory. **c** XRD patterns of the pristine $Cs_{0.05}FA_{0.9}MA_{0.05}PbI_3$ (CsFAMA) perovskite film, the 3F-PEA/CsFAMA heterojunction film prepared by 3-fluoro-phenethylammonium (3F-PEA) ligands dissolved in IPA, and those formed with the addition of DMF, DMSO, DMS, and DES in IPA. Note: the 2θ = 3.0-6.5° range shows independent small-angle XRD characterization. **d**–**g** Time-resolved GIWAXS spectra, tracking the formation of the pristine 3F-PEA/CsFAMA heterojunction (**d**) and the DMS-modulated 3F-PEA/CsFAMA heterojunction (**f**), along with the normalized integrated intensities of the corresponding n = 2 phase (**e**, **g**). Nor.int.intensity is Normalized integrated intensity. **h** Avrami-Erofeev analysis of the $\alpha(t)$ profiles, which describe the temporal evolution of the LD layer formation, was conducted based on the time-dependent integrated intensities of the n = 2 phase extracted from time-resolved GIWAXS profiles of 3F-PEA/CsFAMA heterojunctions with and without DMS addition. **i** Activation energy calculated from temperature-dependent k(T) values using the Arrhenius plot for 3F-PEA/CsFAMA heterojunctions with and without DMS addition.

allows 3F-PEA$^+$ to drive the formation of n = 1 and n = 2 phases, ultimately slowing down the kinetics of LD phase formation, leading to a longer growth period (t_3) (Fig. 1g). The 2D GIWAXS scattering patterns of the formed heterojunction are shown in Supplementary Fig. 6. The slowed dimensional reduction along with longer growth period is expected to improve LD interlayer conformality.

To verify the above analysis, we further conducted time-resolved GIWAXS at different temperatures (Supplementary Figs. 7, 8) and applied the Avrami-Erofeev model to quantify the kinetics of LD layer formation (Supplementary Note 1)[34,35]. The extent of phase development, $\alpha(t)$, was quantified based on the time-dependent integrated intensity of the n = 2 phase peak in GIWAXS. The Avrami exponent n and rate constant k can be determined from the slope and the intercept of the Sharp–Hancock presentation, respectively. As shown in Fig. 1h, the fitted n values for the sample without and with DMS were 0.325 and 0.295, respectively, both less than 1, indicating a diffusion-

https://doi.org/10.1038/s41467-025-64550-4

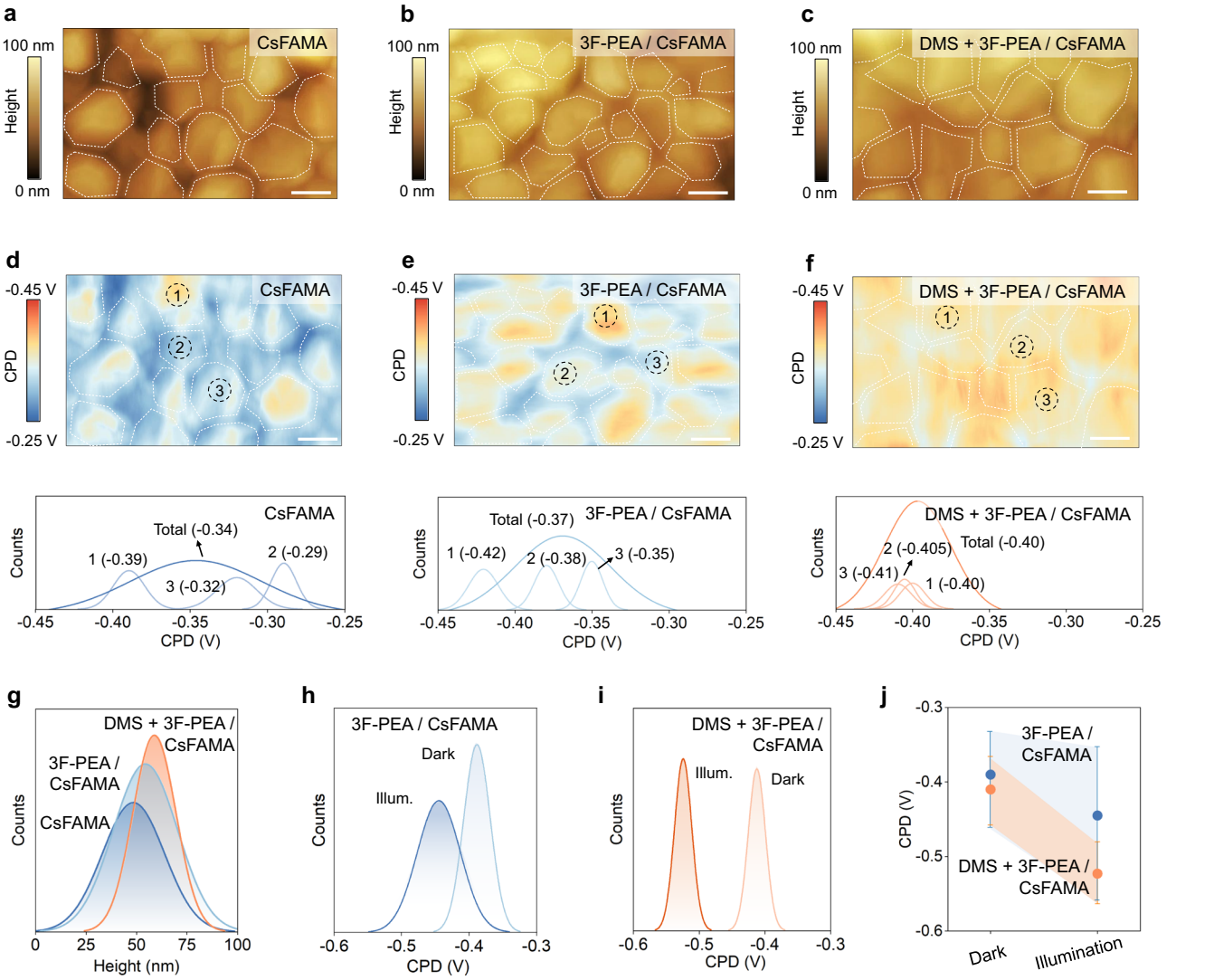

Fig. 2 | Nanoscale analysis of heterojunction homogenization. a–c AFM images of the pristine CsFAMA film (**a**), the 3F-PEA/CsFAMA heterojunction film (**b**), and the DMS-treated heterojunction film (**c**). **d–f** The corresponding KPFM images of the pristine CsFAMA film (**d**), the 3F-PEA/CsFAMA heterojunction film (**e**), and the DMS-modulated heterojunction film (**f**). The bottom of (**d–f**) shows the KPFM potential statistics of the total area and the three selected areas in the KPFM image. The white dashed lines (in **a–f**) outline the perovskite grains. Scale bar: 200 nm. **g** Statistical analysis of the surface roughness of the pristine CsFAMA film, the 3F-PEA/CsFAMA heterojunction films, and the DMS-modulated 3F-PEA/CsFAMA heterojunction film. **h**, **i** Light-intensity-dependent KPFM images of the 3F-PEA/CsFAMA heterojunction and DMS-modulated heterojunction films (~5 nm C_{60} is deposted on the heterojuntion films). The peak intensities in (**h**, **i**) are independent. **j** The corresponding statistical analysis of the light-dependent contact potential difference (CPD) results. Error bars indicate the minimum and maximum values, representing the full range of the statistical data. The shadings highlight the variations in heights and CPDs.

dominated nucleation process[36,37]. The resulting reaction rate constants were 2.61×10^{-3} s^{-1} and 1.13×10^{-3} s^{-1}, confirming a slower LD layer formation rate in the IPA + DMS system. Further analysis based on the Arrhenius equation (Fig. 1i) revealed activation energies of 21.3 and 37.7 kJ/mol for the IPA and IPA + DMS systems, respectively, indicating that DMS effectively modulates the reaction rate by increasing the activation energy[38].

Nanoscale analysis of soft-soft interaction-driven heterojunction homogenization

To elucidate the effect of the retarded reaction rate on the heterojunction structure and electronic homogeneity at the nanoscale, we systematically characterized the heterojunction films using atomic force microscopy (AFM) and Kelvin probe force microscopy (KPFM) as shown in Fig. 2a–g. We also counted the contact potential difference (CPD) in Fig. 2d–f, giving a total value and selected statistical values of the three areas. In the interest of clarity, the heterojunction prepared using IPA is referred to as the 3F-PEA/CsFAMA heterojunction, while the one prepared with IPA + DMS is termed the DMS-modulated 3F-PEA/CsFAMA heterojunction in the following discussion. The pristine CsFAMA film exhibited a coarse grain structure with clear grain boundaries in the AFM images (Fig. 2a), characteristic of typical 3D perovskite films. Correspondingly, in Fig. 2d, the KPFM mapping showed a wide CPD range and noticeable surface potential fluctuations among grains (see CPDs are −0.39 and −0.29 V in areas 1 and 2, respectively), suggesting local electronic inhomogeneities, which are likely attributed to defect states, lattice imperfections, or compositional inhomogeneities[39,40].

For the 3F-PEA/CsFAMA heterojunction, the AFM image showed obvious nanoscale morphological heterogeneity (Fig. 2b), including roughened surfaces and distinct protrusions, indicative of incomplete interfacial coverage. This nanoscale morphological disorder was mirrored in the KPFM results (Fig. 2e), where substantial surface potential variations emerged. The CPD displayed a “patchy” distribution with

pronounced potential jumps between adjacent areas (the CPDs of areas 1, 2, 3 are −0.42, −0.38, and −0.35 V, respectively), suggesting local energy level misalignments. In sharp contrast, the DMS-modulated heterojunction demonstrated a smoother and more continuous surface morphology in the AFM images (Fig. 2c), with minimized height fluctuations (Fig. 2g). Simultaneously, the KPFM mapping (Fig. 2f) exhibited a more uniform surface potential distribution, as confirmed by the narrow statistical spread compared to the non-modulated counterpart. Moreover, the adjacent area showed relatively consistent CPD values (the CPDs of areas 1, 2, 3 are −0.41, −0.405, and −0.40 V, respectively). These results indicate that the introduction of DMS molecules promotes the formation of a more homogeneous 2D interfacial layer. By increasing the activation energy of intercalation, DMS modulation leads to a spatially consistent band structure across the heterojunction.

Furthermore, to compare interfacial charge extraction between the heterojunctions with and without DMS modulation, we deposited a thin (~5 nm) layer of C_{60} onto the heterojunction films and performed KPFM measurements under both dark and illuminated conditions (Supplementary Figs. 9–11). C_{60} serves as an electron extraction layer, allowing evaluation of the energy level alignment and carrier transfer efficiency at the perovskite interface. As shown by the statistical analysis in Fig. 2h–j, the DMS-modulated heterojunction exhibited a larger shift in CPD upon illumination compared to the untreated counterpart. This pronounced CPD shift indicates enhanced photoinduced electron transfer from the perovskite bulk to the C_{60} layer, reflecting more efficient interfacial charge separation. Moreover, after illumination, the CPD distribution of the DMS-modulated heterojunction remained notably narrower than that of the untreated heterojunction, suggesting suppressed local variations in Fermi level position and improved lateral electronic uniformity. These results imply that DMS modulation not only facilitates more effective electron extraction across the heterojunction but also minimizes interfacial energetic disorder. Both factors are critical for reducing interfacial recombination losses and enhancing the overall photovoltaic performance of the device[41–43].

Carrier dynamics

After confirming the morphology and electronic state of the heterojunction surface at the nanoscale, we further conducted spectroscopic analysis on the LD heterojunctions. The prepared heterojunction films were characterized by photoluminescence (PL) mapping at a wavelength of 560 nm (the steady-state PL spectra are provided in Supplementary Fig. 12), corresponding to the n = 2 phase[30,44]. As displayed in Fig. 3a–c, the DMS-modulated 3F-PEA/CsFAMA heterojunction exhibited a more uniform PL intensity across the entire area compared to the pristine 3F-PEA/CsFAMA heterojunction, indicating the formation of a more conformal LD layer on the CsFAMA 3D perovskite surface. Achieving conformal LD coverage is critical to improving stability and reducing interfacial non-radiative recombination[12]. Furthermore, the conformal LD layer can be further supported by the more pronounced shift in the Pb 4*f* peak, along with an increased ratio of C–NH_2 to C = NH_2^+ in the N 1*s* and C 1*s* peaks, as observed in XPS spectra (Supplementary Fig. 13)[45]. Additionally, the Fourier Transform Infrared (FTIR) in Supplementary Fig. 14a demonstrates a characteristic C-F stretching vibration at ~1142 cm^{-1}. Compared to pristine 3F-PEAI, the 3F-PEA/CsFAMA heterojunction exhibits a slight shift of this peak toward higher wavenumbers, suggesting interactions between the 3F-PEAI molecules and the underlying perovskite surface. Further photothermal infrared spectroscopy (PTIR) analysis (Supplementary Fig. 14b, c) reveals that the distribution of F-PEA^+ is similar in films treated with both strategies. This suggests that in the non-conformal 3F-PEA/CsFAMA heterojunction, unincorporated ligands remain on the CsFAMA perovskite surface, potentially acting as passivating agents[12]. As a result, in Fig. 3d–f, the DMS-modulated heterojunction exhibited enhanced PL intensity and homogeneity over a millimeter-scale area when probed at ~810 nm, corresponding to the bulk CsFAMA 3D photoluminescence, indicating improved defect passivation and reduced non-radiative surface recombination.

The defect states and carrier recombination of the heterojunction films were further studied through time-resolved photoluminescence (TRPL) spectroscopy, as shown in Fig. 3g. The PL lifetime fitting revealed a progressive increase in carrier lifetime from 447.8 ns for the pristine CsFAMA perovskite, to 923.3 ns for the 3F-PEA/CsFAMA heterojunction, and to 1896.3 ns for the DMS-modulated 3F-PEA/CsFAMA heterojunction, indicating that the recombination in the pristine perovskite is limited by surface recombination, which is alleviated upon the implementation of LD heterojunctions. Supplementary Fig. 15 shows that the DMS-treated films exhibit a reduced trap-filled limit voltage (V_{TFL}), indicating a lower defect density. Similarly, in Supplementary Fig. 16, the trap density of states (tDOS) of the devices measured using thermal admittance spectroscopy further suggest a reduced trap-state density after DMS modulation[46]. These results all support that the heterojunction with DMS modulation can reduce defect densities and suppress interface non-radiative recombination.

The energy level structures of the pristine CsFAMA perovskite, the 3F-PEA/CsFAMA heterojunction, and the DMS-modulated 3F-PEA/CsFAMA heterojunction were examined using ultraviolet photoelectron spectroscopy (UPS), as shown in Fig. 3h and Supplementary Fig. 17. A progressive decrease in work function was observed in Fig. 3h, starting from the CsFAMA perovskite, followed by the 3F-PEA/CsFAMA heterojunction, and further to the DMS-modulated heterojunction. Simultaneously, the valence band maximum (VBM) shifted from the Fermi level. Although the higher conduction band minimum (CBM) of 3F-PEA-based LD perovskites (n = 1 and 2), resulting from their larger bandgap, which could introduce a potential barrier to electron transport, electrons can tunnel through the ultrathin conformal LD perovskite layer to the C_{60} electron transport layer promoted by band bending, as illustrated in Fig. 3i[47]. Additionally, the energy barrier created by the VBM in the DMS-modulated heterojunction effectively suppresses the recombination of electrons in the conduction band of C_{60} with holes in the valence band of the 3D perovskite owing to the reduced minority charge carrier concentration.

Photovoltaic performance and stability

Figure 4a illustrates the device structure of the fabricated p-i-n PSCs, in which we used NiO_x modified with a mixed [4-(3,6-Dimethyl-9H-carbazol-9-yl)butyl] phosphonic acid (Me-4PACz) and [2-(3,6-dimethoxy-9H-carbazol-9-yl)ethyl] phosphonic acid (MeO-2PACz) hole transport layer and a C_{60} as electron transport layer[48]. The film and device morphologies, along with the photovoltaic performance for optimized DMS concentration, are presented in Supplementary Figs. 18–20. Figure 4b and Supplementary Fig. 21 presents the statistics of the photovoltaic parameters for PSCs based on the pristine CsFAMA perovskite, the 3F-PEA/CsFAMA heterojunction, and the DMS-modulated 3F-PEA/CsFAMA heterojunction. The DMS-modulated 3F-PEA/CsFAMA heterojunction device exhibited the highest average PCE of 26.19%, surpassing the 25.27% of the untreated heterojunction devices and significantly outperforming the 22.81% of the reference devices. Notably, the DMS-modulated heterojunction devices demonstrated the smallest standard deviation (0.26), lower than 0.35 and 0.46 for the other two groups, indicating enhanced reproducibility. This enhanced reproducibility can be primarily attributed to the reduced variation of the V_{OC}, which is a direct result of the ordered and uniform interface formation, linked to the enhanced conformality of LD layer[49].

The *J-V* curves in Fig. 4c further confirm that the DMS-modulated heterojunction devices achieved a champion PCE of 26.70%, with a third-party certified efficiency of 26.47% (Supplementary Fig. 22).

https://doi.org/10.1038/s41467-025-64550-4

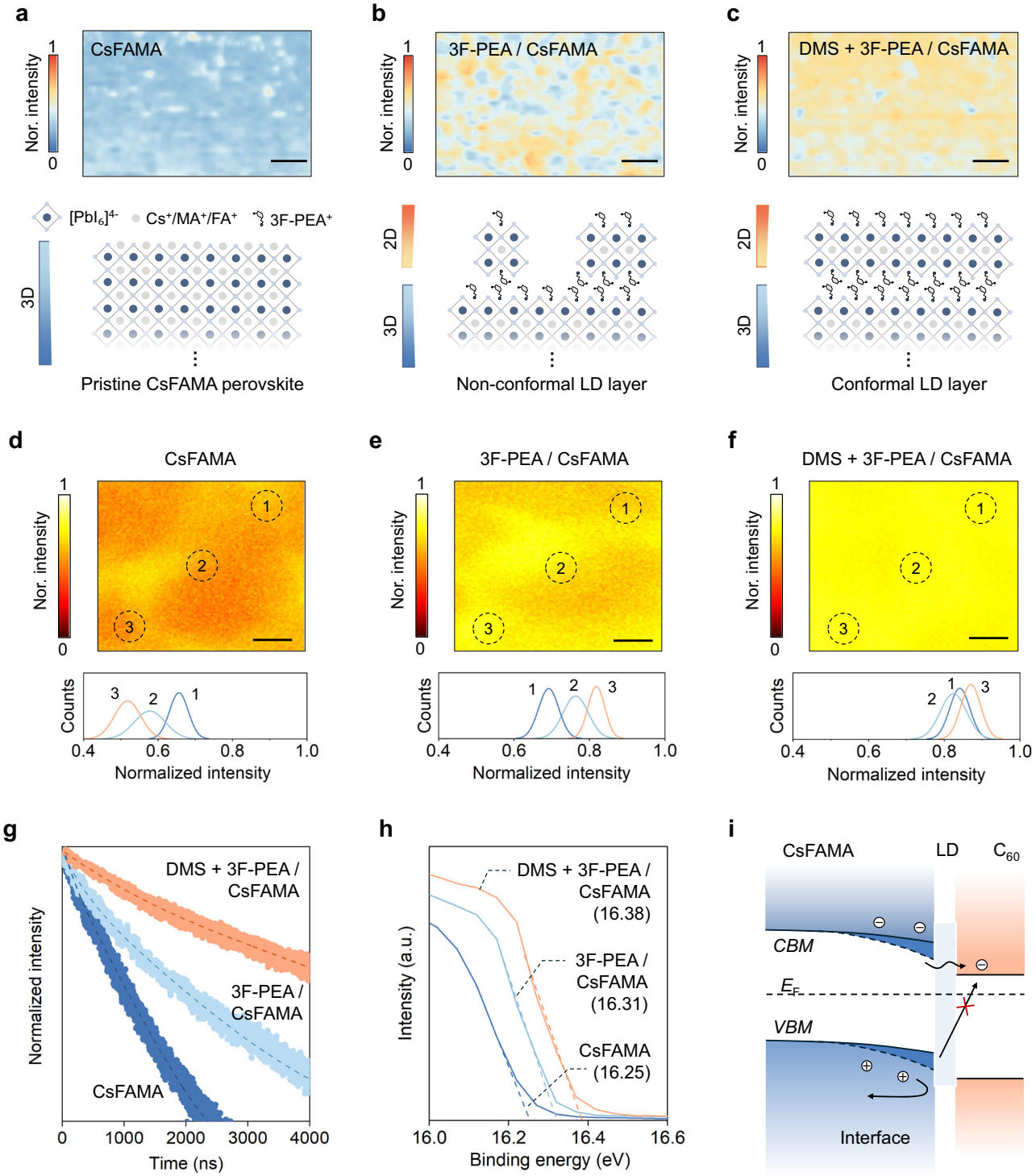

Fig. 3 | Analyses of carrier dynamics. a–c PL mapping of the pristine CsFAMA perovskite (**a**), the 3F-PEA/CsFAMA heterojunction (**b**), and the DMS-modulated 3F-PEA/CsFAMA heterojunction films (**c**) at ~560 nm, corresponding to the n = 2 layer, along with their schematic illustration. Scale bar: 5 μm. Ellipsis represents the continuity of the 3D structure. **d–f** PL mapping images of the films at ~810 nm (corresponding to CsFAMA perovskite). Scale bar: 500 μm. The panels below show the normalized PL intensity distribution corresponding to the labeled areas in the images above. Nor. is Normalized. **g** TRPL spectra of the pristine CsFAMA perovskite film, the 3F-PEA/CsFAMA heterojunction film, and the DMS-modulated 3F-PEA/CsFAMA heterojunction film. The incident laser is from the perovskite surface, and the laser fluence was ~30 nJ/cm^2. **h** UPS spectra of the pristine CsFAMA perovskite film, the 3F-PEA/CsFAMA heterojunction film, and the DMS-modulated 3F-PEA/CsFAMA heterojunction film. **i** Schematic energy level diagram of the heterojunction/C_{60} interface. The solid and dashed lines represent the energy levels before and after DMS modulation, respectively. LD low-dimensional perovskite layer, CBM Conduction Band Minimum, VBM Valence Band Maximum, E_F Fermi level.

https://doi.org/10.1038/s41467-025-64550-4

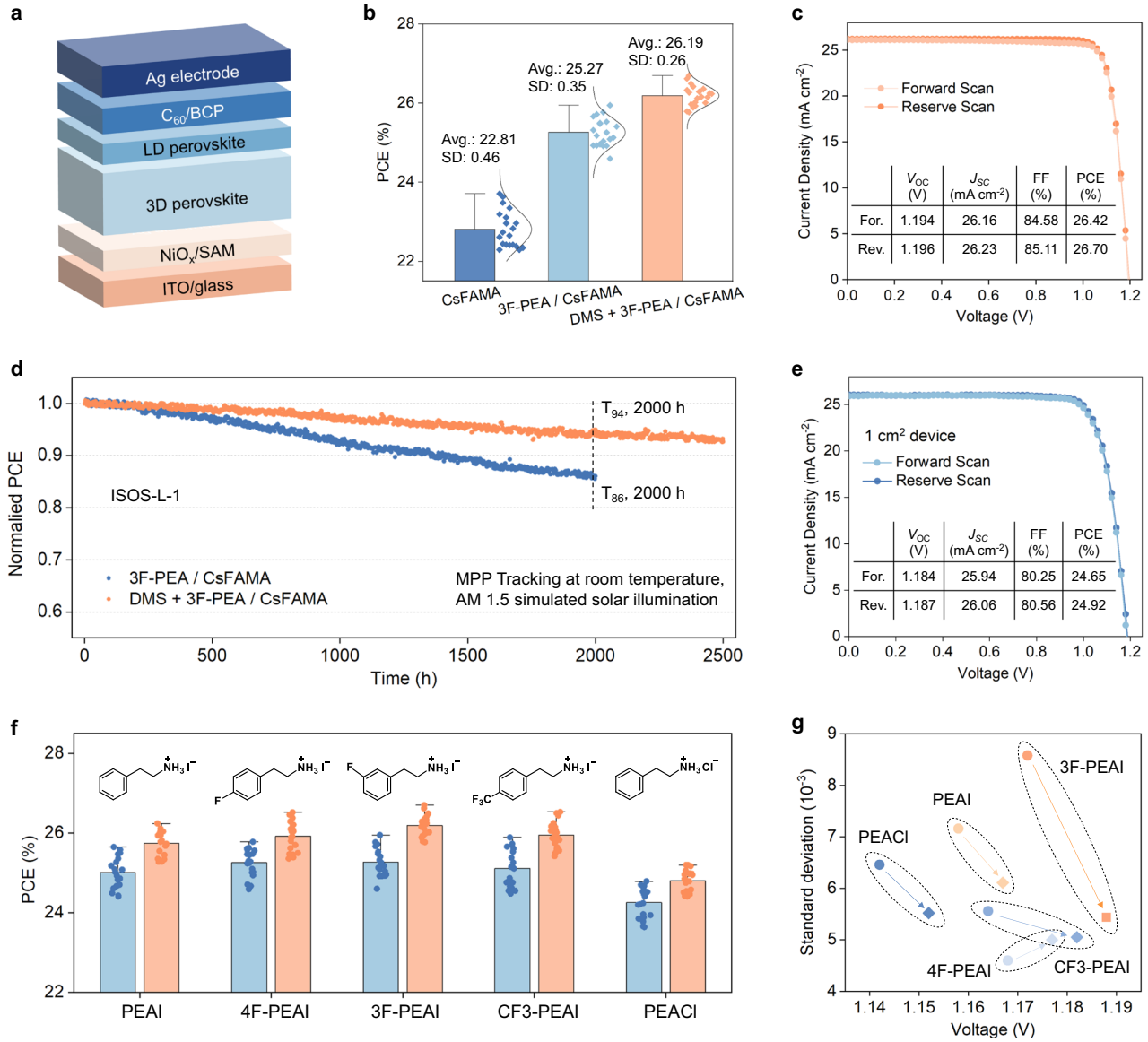

Fig. 4 | Photovoltaic performance and stability. a Schematic illustration of the fabricated p-i-n PSCs. ITO Indium tin oxide, SAM Self-assembled monolayer, 3D Three-dimensional; LD Low-dimensional, BCP Bathocuproine. **b** Photovoltaic performance statistics of the PSCs, based on the pristine CsFAMA perovskite, the 3F-PEA/CsFAMA heterojunction, and the DMS-modulated 3F-PEA/CsFAMA heterojunction. Avg represents the average PCE, and SD is the standard deviation, which are statistically obtained from 20 independent devices. The error bar is the positive deviation beyond 1.5 times the interquartile range (IQR), used to identify upper outliers. **c** *J-V* curves of the best-performing PSCs based on the DMS-modulated heterojunction, measured under forward and reverse scans. **d** Normalized PCE evolution of encapsulated devices, measured at MPP under continuous AM 1.5 G simulated solar illumination at room temperature (RT) in air (under ISOS-L-1 protocol). **e** *J-V* curves of best-performing 1 cm^2 PSCs based on the DMS-modulated heterojunction. **f** PCE statistics of PSCs incorporating different ligands, which include phenethylammonium iodide (PEAI), 4-fluoro-phenethylammonium iodide (4F-PEAI), 3-fluoro-phenethylammonium iodide (3F-PEAI), 4-(trifluoromethyl) phenethylammonium iodide (CF3-PEAI), and phenethylammonium chloride (PEACl), with DMS (orange color) and without DMS (blue color). The error bar is the positive deviation beyond 1.5 times the IQR, used to identify upper outliers. **g** Evolution of *Voc* and its standard deviation in PSCs processed with DMS (Square icons) and without DMS (circle icons) across different ligands, including PEAI, 4F-PEAI, 3F-PEAI, CF3-PEAI and PEACl.

Moreover, the top-performing device exhibited a notable enhancement in open-circuit voltage (V_{OC}), reaching 1.196 V (certified: 1.192 V), and a fill factor (FF) of 85.11% (certified: 84.33%), both exceeding those of the pristine CsFAMA and the untreated heterojunction devices (Supplementary Fig. 23 and Supplementary Table 1). Supplementary Table 2 shows the statistics of state-of-the-art PSCs based on the in-situ fabrication of LD/3D heterojunction, which demonstrates the superiority of this strategy. The external quantum efficiency (EQE) curve of the champion device, shown in Supplementary Fig. 24, aligns closely with the *J-V* measurements, with only a minor discrepancy in the integrated current values. Furthermore, in Supplementary Fig. 25, the DMS-modulated heterojunction achieved an EQE-EL efficiency of 11.76% at an injection current equal to the short-circuit current density, significantly outperforming the pristine CsFAMA perovskite (3.74%) and the untreated heterojunction device (6.23%) under the same conditions. Supplementary Fig. 26 presents the stabilized performance of the DMS-modulated heterojunction, where the stable current density and power output reached 25.13 mA cm^{-2} and 26.39%, respectively. In addition, in Supplementary Fig. 27, we studied the photovoltaic performance of PSCs with DES-modulated heterojunctions and found that, compared with the untreated heterojunction, the performance showed little to no improvement and even declined at higher DES concentrations, consistent with the reduced quality of the LD layers formed.

The long-term stability of the device was further evaluated by testing encapsulated PSCs under MPP operation with continuous AM 1.5 G solar illumination at room temperature in air, following the ISOS-L-1 protocol. As shown in Fig. 4d, devices processed with DMS exhibited superior stability, maintaining 94% of their initial PCE after 2000 h and remaining above 92% after 2500 h. In contrast, untreated devices retained only 86% of their initial efficiency after 2000 h. We used Time-of-Flight Secondary Ion Mass Spectrometry (ToF-SIMS) to study the stability difference of the PSCs after stability tests (Supplementary Fig. 28). Notably, the I^- ion signal in the control device exhibits stronger intensity in the electron transport layer (ETL) compared to the DMS-based devices, indicating more severe iodine migration without DMS modification. This may result from the DMS-induced formation of a more conformal LD layer, which raises the energy barrier for ion migration. In contrast, the inhomogeneous heterojunction in the control group facilitates ion movement, contributing to device performance degradation.

To demonstrate the importance of long range LD layer conformality, we fabricated PSCs with an active area of ~1 cm^2, achieving a highest PCE approaching 25% as shown in Fig. 4e. In comparison, the pristine CsFAMA perovskite and the untreated heterojunction device achieved champion PCEs of 22.56% and 24.19%, respectively (Supplementary Fig. 29). Furthermore, we validated the applicability of this strategy across different LD organic ligands, including phenethylammonium iodide (PEAI), phenethylammonium chloride (PEACl), 4-fluoro-phenethylammonium iodide (4F-PEAI), 4-(trifluoromethyl) phenethylammonium iodide (CF3-PEAI), as well as 3F-PEAI (the study subject above). Their PCEs are summarized in the bar chart in Fig. 4f. Notably, devices processed with DMS consistently exhibited higher PCEs compared to their non-DMS-treated counterparts across all tested LD ligands. Furthermore, almost all PSCs fabricated using the DMS treatment demonstrated reduced standard deviations in PCEs (Supplementary Fig. 30), indicating improved reproducibility. This enhancement can be attributed to the increase in V_{OC} and the reduction of its standard deviation (Fig. 4g and Supplementary Fig. 31), underscoring the effectiveness of DMS modulation in optimizing interfacial layer formation and boosting device performance.

We further incorporated DMS treatment (using 3F-PEAI as the LD ligand) into PSCs with different perovskite compositions, using untreated devices as references. As shown in Supplementary Fig. 32, $Cs_{0.05}FA_{0.95}PbI_3$ PSCs processed with DMS achieved an average PCE of 25.56%, which is higher than that of devices without DMS treatment (24.59%). Also upon adjusting the A-site cation and halide concentration ($Cs_{0.05}FA_{0.90}MA_{0.05}Pb(I_{0.95}Br_{0.05})_3$), the average PCE increased from 24.86% for the pristine heterojunction to 25.74% for the DMS-modulated heterojunction, as shown in Supplementary Fig. 33. Furthermore, tuning the perovskite composition to a wider bandgap ($Cs_{0.15}FA_{0.85}Pb(I_{0.75}Br_{0.25})_3$) reached an average PCE of 23.09% for the DMS-treated devices, outperforming the average value of 22.41% for untreated ones, as shown in Supplementary Fig. 34. The detailed parameters for the champion devices with different compositions are summarized in Supplementary Table 3. These results demonstrate that the DMS modulation is broadly applicable across different perovskite compositions with varied A-site cations and halide ratios, offering a versatile strategy to enhance device performance.

Discussion

In conclusion, we have developed an effective strategy to enhance the uniformity and conformality of the LD interfacial layer through DMS modulation. We demonstrated that DMS can significantly increase the activation energy of LD phase formation and slow down the reaction kinetics of the bulk-to-LD phase transition. This optimization not only broadens the processing window for controlled interfacial layer formation but also facilitates efficient electron extraction from the perovskite absorber to the C_{60} layer, leading to enhanced and more homogeneous charge transport. As a result, the champion PSCs achieved a remarkable PCE of 26.70%, with a certified PCE of 26.48%. Moreover, the devices exhibited excellent operational stability, retaining over 94% of the initial efficiency after 2000 h of MPPT following the ISOS-L-1 protocol. This strategy proves to be general and broadly applicable, with improved PCEs across a range of perovskite compositions and with different organic cations. These findings highlight the pivotal role of soft-soft interactions in governing perovskite heterojunction formation kinetics and establish a general strategy for optimizing LD perovskite interfaces through solvent engineering.

Methods

Materials

Cesium iodide (CsI, 99.999%), methylammonium bromide (MABr, 99.99%) and formamidinium iodide (FAI, 99.99%) were purchased from GreatcellSolar. Lead iodide (PbI_2, 99.99%), lead bromide ($PbBr_2$, 99%), [4-(3,6-Dimethyl-9H-carbazol-9-yl)butyl] phosphonic Acid (Me-4PACz, 99%), and [2-(3,6-Dimethoxy-9H-carbazol-9-yl)ethyl] phosphonic Acid (MeO-2PACz, 98%) were purchased from TCI. C_{60} (99.5%), 3-fluoro-phenylethylammonium iodide (3F-PEAI, 99%), phenethylammonium iodide (PEAI, 99.5%), phenethylammonium chloride (PEACl, 99.5%), 4-fluoro-phenethylammonium iodide (4F-PEAI, 99%), 4-(trifluoromethyl) phenethylammonium iodide (CF3-PEAI, 99%), methylammonium iodide (MAI, 99.9%), methylammonium chloride (MACl, 99.9%), propylammonium chloride (PACl, 99.5%), oleylammonium iodide (OAmI, 98%), 1,8-octanediammonium diiodide (ODADI, 99.5%) and bathocuproine (BCP, 99.9%) were purchased from Xi'an Yuri Solar Co., Ltd. Nickel oxide particle was purchased from Advanced Election Technology Co., Ltd, the average nanoparticle size is 7 nm. The solvents, including dimethylformamide (DMF, 99.8%, anhydrous), dimethyl sulfoxide (DMSO, 99.9%, anhydrous), isopropanol (IPA, 99.5%, anhydrous) and chlorobenzene (CB, 99.8%, anhydrous) were purchased from J&K (China) and used as received. Dimethyl sulfide (DMS, 99%) and Diethyl sulfide (DES, 98%) was purchased from Sigma-Aldrich. High purity silver was purchased from commercial sources. 0.7 mm glass substrates patterned with indium tin oxide (ITO) (15 Ω sq^{-1}) were received from Mishi Tech. Co., Ltd. (China).

Perovskite precursor preparation

1) For $Cs_{0.05}FA_{0.9}MA_{0.05}PbI_3$ precursor preparation, 20.1 mg of CsI, 12.3 mg of MAI, 245.8 mg of FAI, and 750.3 mg of PbI_2 were dissolved in 1 mL of a mixed solvent consisting of DMF and DMSO in a 4:1 volume ratio to make a 1.55 M perovskite precursor solution. 5% excess PbI_2 was used to enhance the photovoltaic performance. Then, 12.5 mol% MACl and 0.4 mol% ODADI were added to the perovskite precursor solution and stir for 10 min.
2) For $Cs_{0.05}FA_{0.95}PbI_3$ precursor preparation, a 1.52 M perovskite precursor solution was prepared by dissolving 19.7 mg of CsI, 254.4 mg of FAI, and 735.8 mg of PbI_2 in 1 mL of a mixed solvent composed of DMF and DMSO in a 4:1 volume ratio. An additional 5% molar excess of PbI_2 was added to enhance the device performance. Then, 10 mol% MACl and 0.3 mol% OAmI were added into the perovskite precursor solution and stir for 10 min.
3) For $Cs_{0.05}FA_{0.9}MA_{0.05}PbI_{2.85}Br_{0.15}$ precursor preparation, 9.1 mg of MABr, 29.7 mg of $PbBr_2$, 21.0 mg of CsI, 256.9 mg of FAI, and 766.3 mg of PbI_2 (8% of excess PbI_2 was needed to improve the device performance) were used in 1 ml DMF:DMSO (4:1 in volume) mixed solvent to make a 1.62 M perovskite precursor solution. Then, add 12.5 mol% MACl and 2 mol% PACl to the perovskite precursor solution and stir for 10 min.
4) For $Cs_{0.15}FA_{0.85}Pb(I_{0.75}Br_{0.25})_3$ (1.68 bandgap) precursor preparation, first dissolve 224.6 mg of FAI, 58.6 mg of CsI, 137.6 mg of $PbBr_2$ and 518.6 mg of PbI_2 in 1 ml DMF:DMSO (4:1 in volume)

mixed solvent to make a 1.50 M perovskite precursor solution. Then, add 10 mol% MACl and 0.3 mol% ODADI to the perovskite precursor solution and stir for 10 min.

PSCs fabrication

Glass/ITO substrates (sheet resistance: 15 Ω sq^{-1}) were sequentially cleaned by ultrasonic treatment in detergent solution, deionized water, acetone, and isopropyl alcohol for 20 min each. After cleaning, the substrates were dried in an oven at 100 °C, followed by oxygen plasma treatment for 10 min to improve surface wettability. Nickel oxide nanoparticles were dispersed in deionized water at a concentration of 10 mg mL^{-1} to prepare a Nickel oxide ink. The resulting dispersion was spin-coated onto the ITO surface at 2500 rpm for 30 s, and subsequently annealed at 150 °C for 30 min under ambient conditions. After annealing, the substrates were transferred into a nitrogen-filled glovebox for further device fabrication. Mix MeO-2PACz at a concentration of 0.3 mg/mL (in methanol) and Me-4PACz at a concentration of 0.3 mg/mL (in methanol) in a 1:3 ratio. Spin-coat the mixture onto substrates at 4000 rpm for 30 s, then anneal at 100 °C for 5 min. Drop 100 µL of the perovskite solution, and then spin-coated at 1000 rpm for 10 s, subsequently at 5000 rpm for 40 s. 300 µL CB was dripped onto films at 5-12 s before the end of spin-coating. The deposited perovskite films were annealed on a hotplate at 100 °C for 30 min.

For the devices with surface treatment, 3F-PEAI (2 mg ml^{-1}) was dissolved in IPA (with a certain amount of DMSO, DMF, DMS and DES addition) and spun on the as-prepared perovskite films at 5000 r.p.m. for 30 s, then annealing at 100 °C for 5 min. All spin-coating procedures were performed inside a nitrogen-filled glovebox, where the ambient temperature was maintained between 18 and 22 °C using an integrated air-conditioning system. During processing, the concentrations of both water and oxygen were strictly controlled to remain below 5 ppm. Subsequently, multilayer deposition was carried out via thermal evaporation under high vacuum conditions (<5×10^{-6} Torr). A 25 nm C_{60} layer was deposited at a rate of 0.5 Å s^{-1}, followed by a 6 nm BCP layer at 0.2 Å s^{-1}, and finally a 100 nm silver electrode at 1.0 Å s^{-1}. To enhance optical transmittance, a 125 nm thick magnesium fluoride layer was thermally evaporated onto the rear side of the ITO substrate at a rate of 1.0 Å s^{-1}. The areas of the two devices are defined by different metal masks as 0.0419 cm^2 and 1 cm^2, respectively.

Characterizations

XRD patterns were recorded using a PANalytical X'Pert Pro diffractometer equipped with a Cu Kα radiation source (λ = 1.5418 Å, 40 kV, 30 mA). Small-angle XRD measurements were performed using a Bruker D8 Venture system to investigate structural ordering at low diffraction angles. XPS was obtained by a PHI VersaProbe II scanning microprobe with a monochromatic Al Kα X-ray source (24.8 W, 100 µm beam size). All binding energies were calibrated with respect to the C 1 s peak at 284.8 eV to correct for charging effects. Surface and cross-sectional morphologies of the perovskite films were examined by SEM using a QUATTROS system (Thermo Fisher Scientific). FTIR spectra were collected using a Tensor 27 spectrometer (Bruker, Germany). PTIR measurements were conducted using a commercial Bruker NanoIR2-FS system, which integrates an AFM operating in contact mode for nanoscale chemical imaging. GIWAXS measurements were carried out at the BL14B1 beamline of the Shanghai Synchrotron Radiation Facility (SSRF), employing X-rays with a wavelength of 0.6887 Å. The incident angle was fixed at 0.3°. A custom-designed sample holder equipped with an integrated heating unit was developed and installed on the GIWAXS sample stage to enable in situ thermal processing. For the time-resolved GIWAXS characterization, the 2D ligand precursor solution is deposited onto a pre-prepared 3D perovskite thin film to ensure full surface wetting. Then, the sample is placed on the custom-made heating holder preheated to 70, 80 and 90 °C. Recordings were made at 0.5 s intervals, and started from the moment the film was placed on the heated holder. The GIWAXS data were analyzed using Fit-2D and presented in q coordinates.

UPS measurements are conducted using the Thermo Fisher Scientific ESCALAB Xi system with a He I discharge lamp. The work function and the valence band edge are determined by analyzing the secondary electron cutoff and the valence band spectra, with the sample biased at −10 V to clearly resolve the cutoff region. KPFM measurements were conducted using a SHIMADZU SPM-9700HT system. The CPD was recorded under both dark and illuminated conditions. For illumination, a white LED light source was positioned at a 15 degree angle above the sample, delivering a power density of 5 mW cm^{-2}. TRPL spectra were recorded using an Edinburgh FLS980 fluorescence spectrometer with an excitation wavelength of 450 nm. PL imaging was conducted using a custom-built confocal microscopy system. Emission signals were collected by an Andor Kymera 329i spectrometer equipped with an Andor 416 CCD detector. For both TRPL and PL imaging measurements, the samples were excited at 450 nm using a monochromatic pulsed laser (pulse width: 6 ps; repetition rate: 78.1 MHz; NKT Photonics SuperK Fianium). The excitation intensity was maintained at 300 W cm^{-2}.

The current-voltage characteristics were conducted in a N_2 glovebox at room temperature by using a Xenon lamp solar simulator (Enlitech, SS-F5). The power of the light was calibrated to 100 mW cm^{-2} by a silicon reference cell (with a KG2 filter). All photovoltaic devices were characterized using a Keithley 2400 source meter under both reverse (1.35 V to −0.1 V) and forward (−0.1 V to 1.35 V) voltage sweep modes, with a scan rate of 0.01 V s^{-1} and a delay time of 10 ms. No preconditioning was applied prior to the measurements. EQE was measured using a Enlight QE-R EQE system. The light intensity was calibrated using a reference photovoltaic solar cell. High-sensitivity EQE measurements were performed using a PECT-600 system (Enlitech, Taiwan), where the photocurrent signal was amplified and modulated via a lock-in amplifier for improved signal-to-noise ratio. EQE_{EL} was evaluated using an ELCT-3010 system (Enlitech, Taiwan) by applying an external voltage or current bias to the device, and the emitted photons were collected and quantified to determine the radiative efficiency.

The long-term operational stability was conducted by following ISOS-L-1 procedure. Before the tests, the PSCs were encapsulated (LT-U001, Luminescence Technology Corp.) with cover glass (0.7 mm). The encapsulated PSCs were operated under 1 sun equivalent LED lamp in the air atmosphere. The PSCs were biased at MPP voltage and the power output was tracked by using a multi-potentiostat (CHI1040C). During the MPP test, the current density-voltage curves of the devices were obtained every 12 h to get the proper loads for the MPP.

Reporting summary

Further information on research design is available in the Nature Portfolio Reporting Summary linked to this article.

Data availability

The data generated in this study are provided in the Supplementary Information/Source Data file. Source data are provided with this paper.

References

1. Zhang, F. et al. Metastable Dion-Jacobson 2D structure enables efficient and stable perovskite solar cells. *Science* **375**, 71–76 (2022).
2. Ye, S. et al. Expanding the low-dimensional interface engineering toolbox for efficient perovskite solar cells. *Nat. Energy* **8**, 284–293 (2023).
3. Jang, Y.-W. et al. Intact 2D/3D halide junction perovskite solar cells via solid-phase in-plane growth. *Nat. Energy* **6**, 63–71 (2021).

4. Sidhik, S. et al. Deterministic fabrication of 3D/2D perovskite bilayer stacks for durable and efficient solar cells. *Science* **377**, 1425–1430 (2022).
5. Gao, D. et al. Long-term stability in perovskite solar cells through atomic layer deposition of tin oxide. *Science* **386**, 187–192 (2024).
6. Liu, C. et al. Two-dimensional perovskitoids enhance stability in perovskite solar cells. *Nature* **633**, 359–364 (2024).
7. Azmi, R. et al. Double-side 2D/3D heterojunctions for inverted perovskite solar cells. *Nature* **628**, 93–98 (2024).
8. Azmi, R. et al. Damp heat-stable perovskite solar cells with tailored-dimensionality 2D/3D heterojunctions. *Science* **376**, 73–77 (2022).
9. Li, B. et al. Harnessing strong aromatic conjugation in low-dimensional perovskite heterojunctions for high-performance photovoltaic devices. *Nat. Commun.* **15**, 2753 (2024).
10. Chang, X. et al. Two-Second-Annealed 2D/3D Perovskite Films with Graded Energy Funnels and Toughened Heterointerfaces for Efficient and Durable Solar Cells. *Angew. Chem. Int. Ed.* **62**, e202309292 (2023).
11. Li, B. et al. Highly efficient and scalable pin perovskite solar cells enabled by poly-metallocene interfaces. *J. Am. Chem. Soc.* **146**, 13391–13398 (2024).
12. Teale, S. et al. Molecular cation and low-dimensional perovskite surface passivation in perovskite solar cells. *Nat. Energy* **9**, 779–792 (2024).
13. Sutanto, A. A. et al. 2D/3D perovskite engineering eliminates interfacial recombination losses in hybrid perovskite solar cells. *Chem* **7**, 1903–1916 (2021).
14. Li, H. et al. 2D/3D heterojunction engineering at the buried interface towards high-performance inverted methylammonium-free perovskite solar cells. *Nat. Energy* **8**, 946–955 (2023).
15. Zhang, S. et al. Minimizing buried interfacial defects for efficient inverted perovskite solar cells. *Science* **380**, 404–409 (2023).
16. Liang, Z. et al. Homogenizing out-of-plane cation composition in perovskite solar cells. *Nature* **624**, 557–563 (2023).
17. Ma, K. et al. Holistic energy landscape management in 2D/3D heterojunction via molecular engineering for efficient perovskite solar cells. *Sci. Adv.* **9**, eadg0032 (2023).
18. Wang, T. et al. Dimensional regulation from 1D/3D to 2D/3D of perovskite interfaces for stable inverted perovskite solar cells. *J. Am. Chem. Soc.* **146**, 7555–7564 (2024).
19. Li, B. et al. Fundamental understanding of stability for halide perovskite photovoltaics: The importance of interfaces. *Chem* **10**, 35–47 (2024).
20. Yang, W. et al. Visualizing interfacial energy offset and defects in efficient 2D/3D heterojunction perovskite solar cells and modules. *Adv. Mater.* **35**, 2302071 (2023).
21. Proppe, A. H. et al. Multication perovskite 2D/3D interfaces form via progressive dimensional reduction. *Nat. Commun.* **12**, 3472 (2021).
22. Quintero-Bermudez, R. et al. Compositional and orientational control in metal halide perovskites of reduced dimensionality. *Nat. Mater.* **17**, 900–907 (2018).
23. Huang, W. et al. Stabilizing high efficiency perovskite solar cells with 3D-2D heterostructures. *Joule* **4**, 975–979 (2020).
24. Huang, Y. et al. Finite perovskite hierarchical structures via ligand confinement leading to efficient inverted perovskite solar cells. *Energy Environ. Sci.* **16**, 557–564 (2023).
25. Proppe, A. H. et al. Synthetic control over quantum well width distribution and carrier migration in low-dimensional perovskite photovoltaics. *J. Am. Chem. Soc.* **140**, 2890–2896 (2018).
26. Li, J. et al. Homogeneous coverage of the low-dimensional perovskite passivation layer for formamidinium-caesium perovskite solar modules. *Nat. Energy* **9**, 1540–1550 (2024).
27. Zhang, F. et al. Buried-interface engineering of conformal 2D/3D perovskite heterojunction for efficient perovskite/silicon tandem solar cells on industrially textured silicon. *Adv. Mater.* **35**, 2303139 (2023).
28. Gutmann, V. Empirical parameters for donor and acceptor properties of solvents. *Electrochim. Acta* **21**, 661–670 (1976).
29. Chen, H. et al. Quantum-size-tuned heterostructures enable efficient and stable inverted perovskite solar cells. *Nat. Photonics* **16**, 352–358 (2022).
30. Chen, P. et al. Multifunctional ytterbium oxide buffer for perovskite solar cells. *Nature* **625**, 516–522 (2024).
31. Tan, Q. et al. Inverted perovskite solar cells using dimethylacridine-based dopants. *Nature* **620**, 545–551 (2023).
32. Zhou, L. et al. Highly efficient and stable planar perovskite solar cells with modulated diffusion passivation toward high power conversion efficiency and ultrahigh fill factor. *Sol. RRL* **3**, 1900293 (2019).
33. Park, S. M. et al. Engineering ligand reactivity enables high-temperature operation of stable perovskite solar cells. *Science* **381**, 209–215 (2023).
34. Moore, D. T. et al. Crystallization kinetics of organic-inorganic trihalide perovskites and the role of the lead anion in crystal growth. *J. Am. Chem. Soc.* **137**, 2350–2358 (2015).
35. Chia, H.-C. et al. Critical intermediate structure that directs the crystalline texture and surface morphology of organo-lead trihalide perovskite. *ACS Appl. Mater. Interfaces* **9**, 36897–36906 (2017).
36. Pradell, T. et al. Diffusion controlled grain growth in primary crystallization: Avrami exponents revisited. *J. Phys.: Condens. Matter* **10**, 3833 (1998).
37. Xu, J. T. et al. Diffusion control of homogeneous crystallization in nanoconfined domains of block copolymers. *J. Macromol. Sci. Part B* **43**, 685–694 (2004).
38. Sánchez, S. et al. Rapid hybrid perovskite film crystallization from solution. *Chem. Soc. Rev.* **50**, 7108–7131 (2021).
39. Chen, H. et al. Regulating surface potential maximizes voltage in all-perovskite tandems. *Nature* **613**, 676–681 (2023).
40. Zhu, H. et al. In situ energetics modulation enables high-efficiency and stable inverted perovskite solar cells. *Nat. Photonics* **19**, 28–35 (2025).
41. Kim, J. et al. Chlorine incorporation in perovskite solar cells for indoor light applications. *Cell Rep. Phys. Sci.* **1**, 100273 (2020).
42. Yang, C. et al. Effects of illumination direction on the surface potential of $CH_3NH_3PbI_3$ perovskite films probed by Kelvin probe force microscopy. *ACS Appl. Mater. Interfaces* **11**, 14044–14050 (2019).
43. Gong, J. et al. Highly efficient all-perovskite photovoltaic-powered battery with dual-function viologen for portable electronics. *Nat. Commun.* **16**, 7980 (2025).
44. Hu, J. et al. Synthetic control over orientational degeneracy of spacer cations enhances solar cell efficiency in two-dimensional perovskites. *Nat. Commun.* **10**, 1276 (2019).
45. Zhou, Q. et al. High-performance perovskite solar cells with enhanced environmental stability based on a (p-$FC_6H_4C_2H_4NH_3)_2[PbI_4]$ capping layer. *Adv. Energy Mater.* **9**, 1802595 (2019).
46. Gao, D. et al. High-efficiency perovskite solar cells enabled by suppressing intermolecular aggregation in hole-selective contacts. *Nat. Photonics*, 1–8 https://doi.org/10.1038/s41566-025-01725-x (2025).
47. Liu, J. et al. Efficient and stable perovskite-silicon tandem solar cells through contact displacement by MgF_x. *Science* **377**, 302–306 (2022).
48. Li, Z. et al. Stabilized hole-selective layer for high-performance inverted p-i-n perovskite solar cells. *Science* **382**, 284–289 (2023).
49. Jiang, Y. et al. Reducing energy disorder in perovskite solar cells by chelation. *J. Am. Chem. Soc.* **144**, 5400–5410 (2022).

Acknowledgements

The work was supported by National Natural Science Foundation of China (52322318), Research Grants Council of Hong Kong Grant

(RFS2526-1S02, R1001-24F, C1055-23G, CRS_CityU104/24, 11308125, N_CityU102/23, 11306521, 11300124, C4005-22Y), Innovation and Technology Fund (ITS/147/22FP, MHP/079/23), the Science Technology and Innovation Committee of Shenzhen Municipality (JCYJ20220818101018038), National Key Research and Development Program of China (No. 2023YFB3809700). B.L. acknowledges the support from the Start-up Project of Central South University (506030113).

Author contributions

B.L., D.G. and F.V. contributed equally to this work. B.L., D.G. and F.V. conceived the ideas and designed the project with Z.Z. Z.Z. directed and supervised the research. B.L. led the research progress, performed characterization, and analyzed the data. D.G. fabricated the devices and conducted the stability tests. F.V. contributed to characterization and data analysis. C.Z., Z.Y., N.W., Jie G., S.L., Jianqiu G. and L.Q. assisted with device fabrication, characterization, and data analysis. Y.-H.L., M.S., and N.J.L. provided scientific insights and contributed to result interpretation. B.L., D.G., F.V., N.J.L. and Z.Z. drafted and finalized the manuscript. All authors reviewed and revised the manuscript.

Competing interests

The authors declare no competing interests.

Additional information

Supplementary information The online version contains supplementary material available at https://doi.org/10.1038/s41467-025-64550-4.

Correspondence and requests for materials should be addressed to Bo Li, Nicholas J. Long or Zonglong Zhu.

Peer review information *Nature Communications* thanks Younghoon Kim and the other anonymous reviewer(s) for their contribution to the peer review of this work. A peer review file is available.